Chemical Science

ROYAL SOCIETY OF CHEMISTRY

EDGE ARTICLE

View Article Online
View Journal | View Issue

Check for updates

Cite this: *Chem. Sci.*, 2020, **11**, 12547

All publication charges for this article have been paid for by the Royal Society of Chemistry

Controlled hierarchical self-assembly of networked coordination nanocapsules *via* the use of molecular chaperones†

Xiangquan Hu,[a] Sisi Feng,*[b] Jialei Du,*[c] Li Shao,[a] Jinxin Lang,[d] Chen Zhang,[e] Steven P. Kelley,[a] Jian Lin,[f] Scott J. Dalgarno,[g] David A. Atwood[h] and Jerry L. Atwood*[a]

Supramolecular chaperones play an important role in directing the assembly of multiple protein subunits and redox-active metal ions into precise, complex and functional quaternary structures. Here we report that hydroxyl tailed *C*-alkylpyrogallol[4]arene ligands and redox-active Mn^{II} ions, with the assistance of proline chaperone molecules, can assemble into two-dimensional (2D) and/or three-dimensional (3D) networked $Mn^{II}_{24}L_6$ nanocapsules. Dimensionality is controlled by coordination between the exterior of nanocapsule subunits, and endohedral functionalization within the 2D system is achieved *via* chaperone guest encapsulation. The tailoring of surface properties of nanocapsules *via* coordination chemistry is also shown as an effective method for the fine-tuning magnetic properties, and electrochemical and spectroscopic studies support that the $Mn^{II}_{24}L_6$ nanocapsule is an effective homogeneous water-oxidation electrocatalyst, operating at pH 6.07 with an exceptionally low overpotential of 368 mV.

Received 9th September 2020
Accepted 16th October 2020

DOI: 10.1039/d0sc05002d

rsc.li/chemical-science

Introduction

Hierarchical self-assembly *via* metal coordination is a ubiquitous process for constructing sophisticated supramolecular structures in nature.[1] As an example of its use in biological systems, metal coordination or bridging plays a crucial role in folding and assembling multiple protein subunits into precise, complex and functional quaternary structures (such as viral metalloproteins).[2,3] Metallosupramolecular assemblies such as metal–organic nanocapsules (MONCs) and/or nanocages are potentially useful models for such complex biological processes,[4,5] and are also promising with regard to energy storage,[6–10] molecular encapsulation,[11–15] catalytic,[16–18] and biomedical applications.[19,20] To date, synthetic chemists have been able to isolate discrete cages consisting of more than 100 precisely designed units through metal coordination.[21] A long-standing challenge, however, is the rational combination of simple components to form hierarchical superstructures with a similar level of assembly complexity as proteins.[22,23] Another challenge that has seldom been addressed in the literature is redox-controlled metal-directed assembly. Albeit at a higher level of complexity, living organisms are able to rapidly select the oxidation state of metal ions such as Cu, Mn and Fe, with regard to protein subunit folding and assembly of quaternary structure, often with the aid of supramolecular chaperones.[24–26] These metallochaperones are typically employed to capture, protect and insert the highly active metal ions into the specific coordination sites before elements of the quaternary structure have formed through subunit self-assembly.[26] The powerful self-assembly approach utilised by biological systems may thus provide access to new hierarchical superstructures (HSSs) with unique properties.

Our group (and others) have used *C*-alkyl-pyrogallol[4]arenes (PgC_n, where *n* is the number of carbon atoms in the pendant alkyl chains), bowl-shaped polydentate macrocycles, to synthesise MONCs *via* metal insertion.[13,27,28] This approach gives rise to large, discrete cages which typically have one of two highly conserved structures: a dimeric cage composed of 2 PgC_ns seamed/bridged by 8 metal ions, or a hexameric cuboctahedral analog comprising 6 PgC_ns and 24 metal ions (the latter of which form 6 triangular faces). These MONCs are readily

[a]Department of Chemistry, University of Missouri-Columbia, 601 S College Ave, Columbia, MO 65211, USA. E-mail: atwood@missouri.edu

[b]Key Laboratory of Chemical Biology and Molecular Engineering of Ministry of Education, Institute of Molecular Science, Shanxi University, Taiyuan 030006, P. R. China. E-mail: ssfeng@sxu.edu.cn

[c]Institute for Advanced Interdisciplinary Research, University of Jinan, Jinan 250022, P. R. China. E-mail: ifc_dujl@ujn.edu.cn

[d]School of Chemistry, Xi'an Jiaotong University, Xi'an 710049, P. R. China

[e]Department of Chemical and Biomolecular Engineering, North Carolina Sate University, Raleigh, North Carolina 27695, USA

[f]Department of Mechanical and Aerospace Engineering, University of Missouri-Columbia, 601 S College Ave, Columbia, MO 65211, USA

[g]Institute of Chemical Sciences, Heriot-Watt University, Riccarton, Edinburgh EH14 4AS, UK

[h]Department of Chemistry, University of Kentucky, Lexington, KY 40506, USA

† Electronic supplementary information (ESI) available. CCDC 1981690 and 1981691. For ESI and crystallographic data in CIF or other electronic format see DOI: 10.1039/d0sc05002d

accessible *via* ambient or solvothermal syntheses using redox stable metal ions such as Zn^{II}, Ni^{II}, Ga^{III}.[28–30] Variations in structure are also possible, for instance by replacing some pyrogallol rings with resorcinol in the PgC_n framework, giving mixed macrocycles that cause 'defects' in the perfect MONC structure.[29] Despite the fact that these two general supramolecular architectures accommodate metals of different size and charge, the controlled assembly of redox-active transition metals has proven difficult. For instance, it has been shown that the reaction of Fe^{II} or Mn^{II} ions with PgC_ns rapidly yielded MONCs with metal ions in mixed oxidation states.[31,32] Indeed, the assembly of mixed-valence MONCs, such as Mn^{II}/Mn^{III}, should be more kinetically favored than solely Mn^{II}-based analogs since Mn^{II} is more thermodynamically stable and kinetically labile than Mn^{III} for coordination.[26] We only recently achieved the assembly of Co^{II} hexameric MONCs by using a route inspired by zinc-finger proteins (ZNFs).[33] In that case the Zn^{II} ion was used to direct assembly of hexameric MONCs that were spontaneously transmetallated with Co^{II} ions to afford the target assembly. Such results indicate that new MONCs with redox-active functionality may (as can be the case with biological systems) require additional templates or chaperones to control their assembly into the correct state.

In this context, we are encouraged to challenge the synthesis of HSSs constructed from *C*-propan-3-ol-pyrogallol[4]arene (PgC_3OH) and coordination-inert but redox-active Mn^{II} ions; the hydroxyl group on PgC_3OH can link MONCs to obtain HSSs.[30] This may not only help to develop a better understanding of the redox-based self-assembly of metalloproteins, but also the construction of HSSs with emergent properties, such as magnetism and catalysis, based on the oxidation state distribution of the metal ions.[34–36] Several reaction conditions and methodologies have been investigated to this end, yet all failed to deliver the selective assembly of any anticipated HSSs (see ESI† for details). We hypothesised that *in situ* redox reactions may prevent the formation of such highly intricate structures.

Herein, we present a design strategy for the construction of such otherwise unobtainable HSSs that uses a reaction system consisting of PgC_3OH, Mn^{II} ions, and proline. The use of proline was inspired by the Mn^{II} coordination sphere in manganese-based proteins, which may effectively capture and stabilise the free metal ion, as well as modulating its weak coordination ability with regard to metal insertion.[26,37,38] We propose a system in which PgC_3OH is assembled into hexameric hydrogen-bonded nanocapsules (MONCs), whilst proline molecules act as the molecular chaperones to capture, protect and insert the Mn^{II} ions into the framework (Scheme 1). Once formed, the thermodynamically and kinetically very stable MONCs serve as subunits (secondary structures) and organise into more complex HSSs through the formation of intermolecular metal–hydroxyl coordination bonds. Using this approach, we obtained 2D and 3D HSSs consisting of Mn^{II}-seamed MONC subunits (**1**, $[Mn_{24}(PgC_3OH)_6(H_2O)_{44}]$ and **2**, $[Mn_{24}(PgC_3OH)_6(H_2O)_{44}(CH_3CN)_2]$), structurally controlled by subtle changes in reaction conditions.

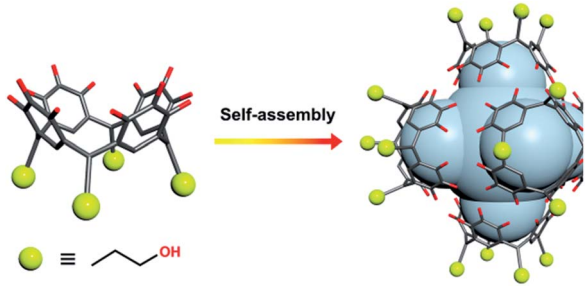

Scheme 1 Pre-assembly strategy of Mn^{II}-seamed MONC subunits used in this study. Color codes: carbon, grey; oxygen, red; Mn^{II}, purple.

Results and discussions

Compound **1** has been studied and characterised by scanning electron microscopy images (Fig. S1†), single-crystal X-ray diffraction (SC-XRD, Fig. S2†), FT-IR (Fig. S3†), elemental analysis (EA), MALDI-TOF MS (Fig. S4†), thermogravimetric analysis (TGA, Fig. S5†) and differential scanning calorimetry (DSC, Fig. S6†), details of which can be found in the ESI.† Compound **1** crystallises in the monoclinic space group $P2_1/n$. The crystal structure of **1** shows a 2D framework constructed from infinite MONCs subunits, with each MONC being assembled from 30 components: six PgC_3OH molecules and 24 metal ions (Fig. 1). The overall geometry of the MONC subunit corresponds to that of a truncated octahedron, which is similar to the previously reported hexameric MONCs.[28] Each hexagonal face of the MONC is capped by one $[Mn_3O_3]$ trimetallic cluster with Mn–O distances in the range of 2.03–2.11 Å, Mn–O–Mn angles in the range of 133.17–137.50°, and O–Mn–O angles in the range of 99.34–105.66°. All Mn^{II} ions adopt an octahedral ligand field, where the equatorial positions are coordinated with oxygen atoms from the upper-rim of PgC_3OH units. Bond-valence sum (BVS) analysis, coupled with examination of bonding energy reveals that all Mn ions are in the +2 oxidation state (Table S1 and Fig. S7†). Interestingly, each MONC encapsulates two proline chaperone ligands that coordinate in

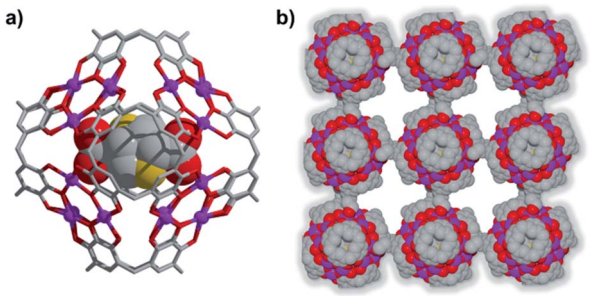

Fig. 1 (a) Side and (b) extend views of the single crystal X-ray structure of **1**. Inspection shows 2D HSSs composed of Mn^{II}-MONC subunits, each of which encapsulates two proline chaperone molecules *via* metal coordination. Color codes: manganese (purple), carbon (grey), oxygen (red), nitrogen (yellow). Hydrogen atoms, axial water ligands and hydroxyl tail alkyl chains not involved in metal–ligand coordination to adjacent MONC subunits were removed for clarity.

a bridging mode between two Mn^{II} ions (metal–carboxyl distances in the range of 2.24–2.27 Å). This suggests that the proline molecules perform the critical function of a molecular chaperone, capturing, protecting and inserting Mn^{II} ions into MONCs *via* ligand exchange during the assembly process. The extended view of **1** shows that each MONC is connected to four adjacent symmetry equivalents *via* double manganese–hydroxyl coordination (M–O distances: 2.26–2.35 Å). One MONC provides a hydroxyl tail and a metal coordination site for another, and the other axial positions are occupied by water molecules.

Introduction of a greater amount of water to similar reaction conditions as those used in the synthesis of **1** changed both the internal and external properties of the Mn^{II}-seamed MONCs, resulting in the formation of a 3D HSSs which crystallises in an orthorhombic system (structure solution in space group *Pccn*, **2**, Fig. 2, Table S2 and Fig. S8–S10†). On the internal surface, all axial positions at the metal centres are occupied by water molecules, whilst inspection of the exterior reveals that each MONC subunit is linked to eight symmetry equivalents *via* single manganese–hydroxyl coordination bonds (two crystallographic M–O distances: 2.276 and 2.279 Å, respectively), the result being assembly into a cubic tertiary structure (Fig. 2b). This supramolecular nanocube is assembled from 216 Mn^{II} ions and 54 PgC_3OH macrocyclic ligands and has an edge of 4.5 nm. Within the nanocube there are two types of MONC subunits with different orientation in the solid lattice, highlighted by the disparate colours in Fig. 2. This structural motif is similar to the unit cell of CsCl (Fig. 2c), and the extended view exhibits a hierarchical CsCl-like superstructure (Fig. 2d).

Magnetic susceptibility data for **1** and **2** were recorded in the temperature range of 2.0–300 K in an applied magnetic field of 1000 Oe. The χ_m, $\chi_m T$ *vs.* T plots for the complexes are shown in

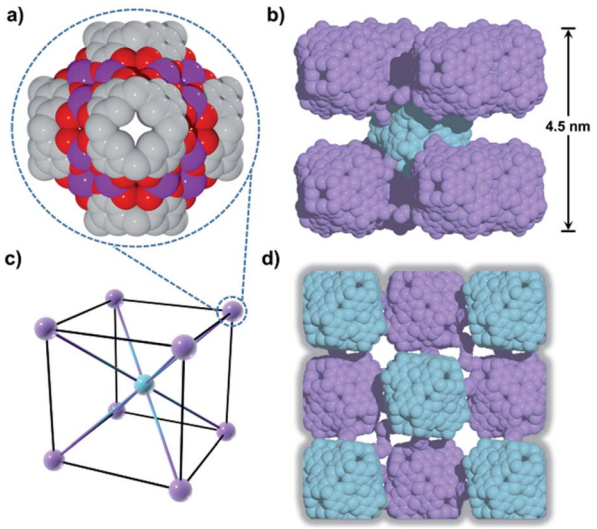

Fig. 2 (a) Mn^{II}-seamed MONC subunits (secondary structure). (b) Supramolecular nanocubes (tertiary structure). (c) CsCl unit cell and (d) the 3D hierarchical CsCl-like superstructure (quaternary structure). Hydrogen atoms, axial ligands and hydroxyl tail alkyl chains not involved in metal–ligand coordination to adjacent MONC subunits were removed for clarity.

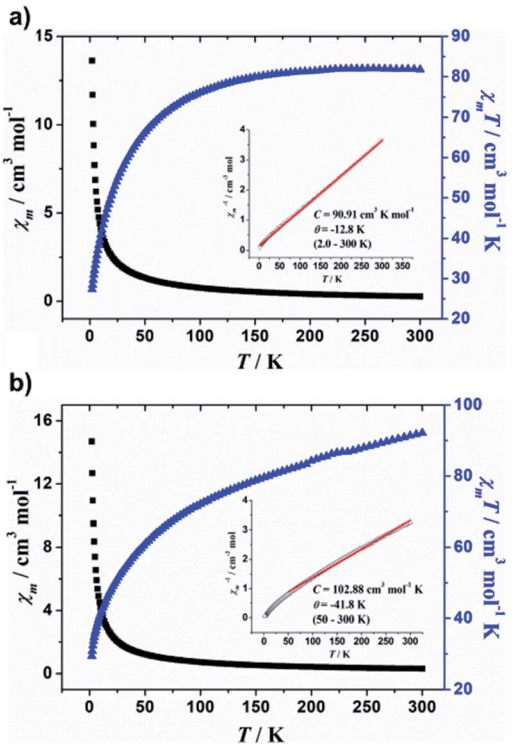

Fig. 3 Temperature dependence of χ_m, $\chi_m T$, and χ_m^{-1} (inset) collected in applied field of 1000 Oe for (a) **1** and (b) **2**. Red solid line represents best fits.

Fig. 3, where χ_m is the molar magnetic susceptibility. For supramolecular assemblies **1** and **2**, the values of $\chi_m T$ at 300 K are 81.8 and 92.2 cm^3 mol^{-1} K, respectively, but lower than that of expected for the sum of the Curie constants for 24 non-interacting Mn^{II} (s = 5/2) ions, with g = 2.00 (105.0 cm^3 mol^{-1} K). Upon cooling, $\chi_m T$ first gradually decreases to a value of 76.1 cm^3 K mol^{-1} at 100 K, and then decreases more rapidly on further cooling to 27.3 cm^3 K mol^{-1} at 2.0 K for **1**, however, $\chi_m T$ decreases to the minimum value of 29.4 cm^3 mol^{-1} K at 2.0 K for **2**, indicating antiferromagnetic coupling within the Mn^{II} ions. Above 50 K, the temperature dependence of χ_m^{-1} obeys the Curie–Weiss law with $C = 90.91$ cm^3 K mol^{-1} and $\theta = -12.8$ K above 2.0 K for **1** and $C = 102.88$ cm^3 mol^{-1} K and $\theta = -41.8$ K for **2** (see Fig. 3, inset). The negative θ values confirm the antiferromagnetic coupling within the Mn^{II} ions and the antiferromagnetic coupling in **2** is stronger than that in **1**. Furthermore, the shapes of the M/H plots are quite like that of the antiferromagnet, in which the M values increase rapidly at low fields, with no obvious saturation observed up to 70 kOe (Fig. S11 and 12†).

Water oxidation (WO, $2H_2O \rightarrow O_2 + 4H^+ + 4e^-$) is regarded as a key half-reaction for solar fuel production.[39] The rational design and synthesis of cheap, efficient and stable water-oxidising catalysts are significant challenges in science and technology.[40] In nature, the oxygen-evolving complex (OEC, a $CaMn_4O_5$ cluster) in photosystem II (PS II) can efficiently oxidize water.[41] It has been shown that the Mn^{IV}–O–Mn^{III}–H_2O motif plays a crucial role in the activity of the OEC and its

mimics.[42] Inspired by the OEC, several Mn clusters have been used as structural mimics. In particular, the presence of high oxidation state +3 and +4 Mn ions and four water binding sites have been applied for electrocatalytic oxidation of water, examples such as $Mn_{12}O_{12}(OAc)_{16-x}L_x(H_2O)_4$ (L = acetate, benzoate, benzenesulfonate, diphenylphosphonate, and dichloroacetate).[43–45] However, the catalytic activity of these biomimetic Mn-based clusters for water oxidation was shown to be hindered by either high overpotentials (ranging from 640–820 mV) or low structural stability.[40] Kinetically and thermodynamically very stable Mn clusters assembled with exclusively Mn^{II} ions may solve one of such problem even though a series of mononuclear manganese complexes $[(Py_2NR_2)Mn^{II}(H_2O)_2]^{2+}$ (R = H, Me, *t*Bu) were reported to be active in electrocatalytic water oxidation with an relatively high overpotential of approximately 800 mV (FTO working electrode).[34] However, to the best of our knowledge it remains unknown whether polynuclear Mn^{II} clusters are capable of being highly active with respect to water oxidation.

This long-standing question has been examined with **1** and **2** using electrochemical techniques. Crystals of **1** and **2** were dissolved in 0.1 M aqueous acetate buffer at pH 6.07 *via* sonochemistry, the pH at which the OEC within PSII shows optimal catalytic performance.[46] The resulting solutions of **1** and **2** were subjected to UV-Vis spectroscopy and showed two broad absorption bands at around λ_{max} = 262 and 315 nm for **1** and λ_{max} = 260 and 312 nm for **2**, which can be assigned to the π–π* transition and ligand-to-metal charge transfer transition, respectively (Fig. S13†). The redox peaks associated with manganese of **1** and **2** in aqueous acetate buffer have been detected *via* cyclic voltammetry (Fig. 4a, b and S14†). These corresponded to the oxidation of Mn^{2+} to Mn^{4+} (E = 0.87 V) and the reduction of Mn^{4+} to Mn^{3+} (E = 0.83 V), Mn^{4+} to Mn^{2+} (E = 0.55 V), and Mn^{3+} to Mn^{2+} (E = 0.26 V).[47] The solution stability of the coordination structures was investigated using dynamic light scattering (DLS) techniques. It was shown that sonication of these solutions resulted in the formation of species in the size range of 2–3 nm, corresponding to the molecular hydrodynamic diameter of discrete MONCs (Fig. S15†),[13] and implying that HSSs converted into discrete MONCs; we envisage that some metal-coordinated hydroxyl groups of PgC_3OH moieties on axial positions may be displaced by water molecules. Interestingly, upon evaporation of an aqueous acetate buffer solution of **1** and **2**, spherical, micron-scale metallosuperstructures were observed by SEM (Fig. 4c, d and S16†). FT-IR and small angle X-ray scattering studies further supported that they were composed of many MONC subunits (Fig. S17 and 18†). We propose that the hierarchical metal–organic micron spheriods (MOMSs) may be stabilized by a large number of van der Waals interactions between neighboring alkyl chains and hydrophilic regions of the discrete MONCs.

Furthermore, cyclic voltammograms (CVs) clearly indicated that water oxidation can be catalyzed by both **1** and **2** (Fig. 5).[43,47] Water oxidation occurs at an exceptionally low overpotential of only 368 mV. This is higher than that of the current state-of-art Ru-bda complex (bda = 2,2′-bipyridine-6,6′-dicarboxylate, 180 mV at pH 7), illustrating that there is still room for further improvements.[48] Continuous CV scan experiments and bulk electrolysis of **1** and **2** demonstrated that these electrocatalysts have high catalytic activity and stability toward water oxidation (Fig. S19 and 20†). UV-Vis and DLS measurements taken after electrolysis of **1** and **2** showed that the waves and particle size are retained (Fig. S21 and 22†). Moreover, the MOMSs re-formed and could be detected upon evaporation of the catalyst solution in subsequent SEM studies (Fig. S23†). Collectively, these measurements suggest that the MONC subunit is a homogeneous water oxidation electrocatalyst. This result may thus provide a new strategy for the design and synthesis of cheap, efficient and stable water-oxidizing catalysts since it first suggests that soluble Mn^{II} clusters may be used to effectively facilitate the oxidation of water, despite the enormous efforts made to mimic the $CaMn_4O_5$ cluster to date. We further envision that improvements of catalyst stability and activity may be possible. This may be achieved through (for example) attaching appropriate axial ligands to the constituent metal ions, or functionalizing alkyl chains on the MONC surface. In addition, other soluble metal-seamed dimeric or hexameric MONCs, such as those formed with Fe^{II}, Co^{II} and Cu^{II} ions, are also promising with regard to electrocatalytic water oxidation.[36]

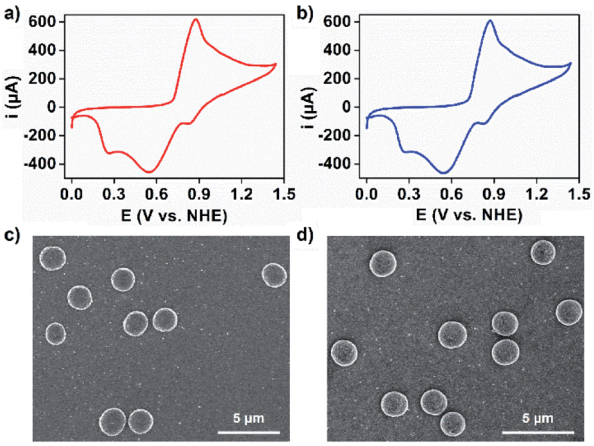

Fig. 4 Cyclic voltammograms (CVs) of (a) **1** and (b) **2** (0.5 mM) in 0.1 M acetate buffer at pH 6.07 using an FTO (S = 1 cm^2) working electrode. Scan rate is 50 mV s^{-1}. SEM images of hierarchical micron spheroids formed from an aqueous acetate buffer of (c) **1** and (d) **2**.

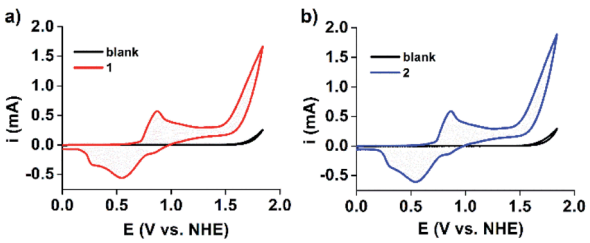

Fig. 5 CV scans of (a) **1** and (b) **2** (0.5 mM, 50 mV s^{-1} scan rate) in 0.1 M acetate buffer at pH 6.07. For comparison, CVs of the blank buffer are also shown. FTO (S = 1 cm^2) was used as the working electrode.

Conclusions

In summary, we have developed a new strategy for the rational construction of HSSs using biomimetic self-assembly as the synthetic methodology. Akin to the self-assembly behaviours of protein subunits with redox-active metal ions, the assembly of these sophisticated supramolecular architectures has been accomplished by employing proline molecules as molecular chaperones to selectively insert redox-active Mn^{II} ions into the coordination sites of a pre-assembled ONC skeleton, which further directs the Mn^{II}-seamed MONC subunits to fold and assemble into more complex HSSs across different dimensionality. This is achieved *via* control of both interior and/or exterior surface properties of the MONC subunits, through coordination and host–guest chemistries, also allowing for the fine-tuning of magnetic properties. The catalytic activity and stability of $Mn^{II}_{24}L_6$ MONCs toward homogeneous water oxidation at pH 6.07 with an exceptionally low overpotential of only 368 mV is noteworthy.

Overall, this approach represents an important advancement in supramolecular chemistry by design. Further efforts will be invested in the design and synthesis of extremely challenging and complex HSSs with other redox-active or coordinatively inert metal ions (*e.g.* Cr^{II}/Cr^{III} and Fe^{II}/Fe^{III}), as well as inserting suitably functionalized guest molecules for potential application in the areas of molecular electronics/magnets and catalysis, all of which may be modulated by appropriate molecular chaperones. Finally, this strategy may be widely exploited in the rational design and synthesis of other metal–organic systems, such as metal–organic cages (MOCs), polyhedra (MOPs) or artificial metalloproteins, the properties and/or functions of which can be subsequently tailored accordingly.

Conflicts of interest

The authors declare no conflict of interest.

Acknowledgements

We thank University of Missouri for financial and research facility support of this work. We thank the U.S. National Science Foundation for support of this work (1825352). This work was also partially supported by the Natural Science Foundation of Shandong Province (ZR2018BB035, 2019GSF109013), Shanxi Province (201701D121039).

Notes and references

1 T. Zhou, D. H. Hendrickson, Q. J. Sattentau and P. D. Kwong, *Proc. Natl. Acad. Sci. U. S. A.*, 2005, **102**, 14575–14580.
2 Y. Lu, N. Yeung, N. Sieracki and N. M. Marshall, *Nature*, 2009, **460**, 855–862.
3 E. N. Salgado, R. J. Radford and F. A. Tezcan, *Acc. Chem. Res.*, 2010, **43**, 661–672.
4 R. A. Bilbeisi, T. K. Roson and J. R. Nitschke, *Angew. Chem., Int. Ed.*, 2013, **52**, 9027–9030.
5 J. L. Atwood, L. J. Barbour, S. J. Dalgarno, M. J. Hardie, C. L. Raston and H. R. Webb, *J. Am. Chem. Soc.*, 2004, **126**, 13170–13171.
6 T. R. Cook, Y. Zheng and P. J. Stang, *Chem. Rev.*, 2013, **113**, 734–777.
7 Z. Niu, S. Feng, X. Liu, J. Ma, S. Ma and P. Cheng, *J. Am. Chem. Soc.*, 2015, **137**, 14873–14876.
8 J. J. Perry IV, J. A. Perma and M. J. Zaworotko, *Chem. Soc. Rev.*, 2009, **38**, 1400–1417.
9 T.-F. Liu, P.-Y. Chen, A. A. Yakovenko and H.-C. Zhou, *J. Am. Chem. Soc.*, 2012, **134**, 17358–17361.
10 H. Furukawa, J. Kim, N. W. Ockwig, M. O'Keeffe and O. M. Yaghi, *J. Am. Chem. Soc.*, 2008, **130**, 11650–11661.
11 D. Zhang, T. K. Roson and J. R. Nitschke, *Acc. Chem. Res.*, 2018, **51**, 2423–2436.
12 H. Kumari, C. A. Deakyne and J. L. Atwood, *Acc. Chem. Res.*, 2014, **47**, 3080–3088.
13 S. Chakraborty and G. R. Newkome, *Chem. Soc. Rev.*, 2018, **47**, 3991–4016.
14 M. Yoshizawa and L. Catti, *Acc. Chem. Res.*, 2019, **52**, 2392–2404.
15 K. Harris, D. Fujita and M. Fujita, *Chem. Commun.*, 2013, **49**, 6703–6712.
16 C. J. Brown, F. D. Toste, R. G. Bergman and K. N. Raymond, *Chem. Rev.*, 2015, **115**, 3012–3035.
17 Y. Inokuma, M. Kawano and M. Fujita, *Nat. Chem.*, 2011, **3**, 349–358.
18 Y. Yu and J. Rebek, *Acc. Chem. Res.*, 2018, **51**, 3031–3040.
19 H. Sepehrpour, X. Fu, Y. Sun and P. J. Stang, *J. Am. Chem. Soc.*, 2019, **141**, 14005–14020.
20 Y. Fang, X. Lian, Y. Huang, G. Fu, Z. Xiao, Q. Wang, B. Nan, J.-P. Pellois and H.-C. Zhou, *Small*, 2018, **14**, 1802709.
21 Q. Sun, J. Iwasa, D. Ogawa, Y. Ishido, S. Sato, T. Ozeki, Y. Sei, K. Yamaguchi and M. Fujita, *Science*, 2010, **328**, 1144–1147.
22 P. F. Damasceno, M. Engel and S. C. Glotzer, *Science*, 2012, **337**, 453–457.
23 L. Peng, N. A. Vermeulen, C. D. Malliakas, D. A. Gomez-Gualdron, A. J. Howarth, B. L. Mehdi, A. Dohnalkova, N. D. Browning, M. O'Keeffe and O. K. Farha, *Science*, 2017, **356**, 624–627.
24 L. A. Finney and T. V. O'Halloran, *Science*, 2003, **300**, 931–936.
25 A. C. Rosenzweig, *Chem. Biol.*, 2002, **9**, 673–677.
26 J. W. Whittaker, *Biochim. Biophys. Acta*, 2010, **2**, 298–307.
27 K. Su, M. Wu, D. Yuan and M. Hong, *Nat. Commun.*, 2018, **9**, 1–6.
28 S. J. Dalgarno, N. P. Power and J. L. Atwood, *Coord. Chem. Rev.*, 2008, **252**, 825–841.
29 D. A. Fowler, A. S. Rathnayake, S. Kennedy, H. Kumari, C. M. Beavers, S. J. Teat and J. L. Atwood, *J. Am. Chem. Soc.*, 2013, **135**, 12184–12187.
30 C. Zhang, R. S. Patil, C. Liu, C. L. Barnes, T. Li and J. L. Atwood, *J. Am. Chem. Soc.*, 2017, **139**, 2920–2923.
31 A. S. Rathnayake, H. W. L. Fraser, E. K. Brechin, S. J. Dalgarno, J. E. Baumeister, J. White, P. Rungthanaphatsophon, J. R. Walensky, C. L. Barnes, S. J. Teat and J. L. Atwood, *Nat. Commun.*, 2018, **9**, 1–6.

32 A. S. Rathnayake, H. W. L. Fraser, E. K. Brechin, S. J. Dalgarno, J. E. Baumeister, J. White, P. Rungthanaphatsophon, J. R. Walensky, S. P. Kelley, C. L. Barnes and J. L. Atwood, *J. Am. Chem. Soc.*, 2018, **140**, 15611–15615.
33 X. Hu, J. Chai, C. Zhang, J. Lang, S. P. Kelley, S. Feng, B. Liu, D. A. Atwood and J. L. Atwood, *J. Am. Chem. Soc.*, 2019, **141**, 9151–9154.
34 G. Karotsis, S. J. Teat, W. Wernsdorfer, S. Pilligkos, S. J. Dalgarno and E. K. Brechin, *Angew. Chem., Int. Ed.*, 2009, **48**, 8285–8288.
35 P. Dechambenoit and J. R. Long, *Chem. Soc. Rev.*, 2011, **40**, 3249–3265.
36 W.-T. Lee, S. B. Munoz, D. A. Dickie and J. M. Smith, *Angew. Chem., Int. Ed.*, 2014, **53**, 9856–9859.
37 K. J. Waldron, J. C. Rutherford, D. Ford and N. J. Robinson, *Nature*, 2009, **460**, 823–830.
38 J. R. Calhoun, F. Nastri, O. Maglio, V. Pavone, A. Lombardi and W. F. DeGrado, *J. Pept. Sci.*, 2005, **80**, 264–278.
39 K. J. Young, B. J. Brenan, R. Tagore and G. W. Brudvig, *Acc. Chem. Res.*, 2015, **48**, 567–574.
40 A. I. Nguyen, *Proc. Natl. Acad. Sci. U. S. A.*, 2019, **116**, 11630–11639.
41 S. Mukhopadhyay, S. K. Mandal, S. Bhaduri and W. H. Armstrong, *Chem. Rev.*, 2004, **104**, 3981–4026.
42 A. K. Poulsen, A. Rompel and C. J. McKenzie, *Angew. Chem., Int. Ed.*, 2005, **44**, 6916–6920.
43 Y. Mousazade, M. R. Mohammadi, P. Chernev, R. Bikas, R. Bagheri, Z. Song, T. Lis, H. Dau and M. M. Najafpour, *Catal. Sci. Technol.*, 2018, **8**, 4390–4398.
44 Y. Yan, L. S. Lee and A. A. Ruddy, *Inorg. Chem.*, 2015, **54**, 4550–4555.
45 G. Maayan, N. Gluz and G. Christou, *Nat. Catal.*, 2018, **1**, 48–54.
46 H. Schiller and H. Dau, *J. Photochem. Photobiol., B*, 2000, **55**, 138–144.
47 Y. Du, Z. Fu and L. Bi, *Dalton Trans.*, 2018, **47**, 7282–7289.
48 B. Zhang and Li. Sun, *J. Am. Chem. Soc.*, 2019, **141**, 5565–5580.

Supporting Information

Controlled hierarchical self-assembly of networked coordination nanocapsules via the use of molecular chaperones

Xiangquan Hu[1], Sisi Feng[2]*, Jialei Du[3]*, Li Shao[1], Jinxin Lang[4], Chen Zhang[5], Steven P. Kelley[1], Jian Lin[6], Scott J. Dalgarno[7], David A. Atwood[8] and Jerry L. Atwood[1]*

[1] Department of Chemistry, University of Missouri-Columbia, Columbia MO 65211, USA

[2] Key Laboratory of Chemical Biology and Molecular Engineering of Ministry of Education, Institute of Molecular Science, Shanxi University, Taiyuan 030006, P. R. China

[3] Institute for Advanced Interdisciplinary Research, University of Jinan, Jinan 250022, P. R. China

[4] School of Chemistry, Xi'an Jiaotong University, Xi'an 710049, P. R. China

[5] Department of Chemical and Biomolecular Engineering, North Carolina Sate University, Raleigh, North Carolina 27695, USA

[6] Department of Mechanical and Aerospace Engineering, University of Missouri-Columbia, Columbia MO 65211, USA

[7] Institute of Chemical Sciences, Heriot-Watt University, Riccarton, Edinburgh EH14 4AS, United Kingdom

[8] Department of Chemistry, University of Kentucky, Lexington, KY 40506, USA

*Corresponding author: ssfeng@sxu.edu.cn, ifc_dujl@ujn.edu.cn, atwoodj@missouri.edu

This file includes:

Figures S1 to S23

Tables S1 to S2

References 1 to 15

1. Materials and Methods.

All solvents and chemicals were purchased from Sigma-Aldrich or Fisher Laboratories and used without further purification. Notably, manganese (II) nitrate tetrahydrate crystals were stored in glovebox at 23°C. The solvents were dried by 3Å molecular sieves for uses of solvothermal synthesis. All combinations of PgC_3OH macrocycles and manganese salts were carried out using glovebox techniques at 23°C. All pH measurements were performed using a Thermo Scientific Orion Star A111 Benchtop pH Meter. Powder X-ray Diffraction data was collected on a Bruker Apex II CCD diffractometer at room temperature using Cu (Kα) radiation Inco-tech Microfocus II (1.5406Å). Powder X-ray diffraction was measured on a Bruker X8 Prospector single crystal X-ray diffractometer equipped with an IμS microfocus Cu-Kα X-ray source (λ = 1.54106 Å, power = 40 kV, 0.65 mA). Dry samples were hand-ground into powder and loaded directly into the tubing. Data collection was performed with the area detector and X-ray source fixed, and the tubing containing the sample at a 90° angle to the X-ray beam at a sample-to-detector distance of 8.00 cm. The samples were rotated 360° along the axis of the tubing during collection. Each data set was composed of a series of 2-minute long scans across the 2-theta range of 2.5 to 40°. Photographic data were reduced by integrating along a 77°-wide sector from 2.5 to 35° 2-theta in 0.02° slices along 2-theta. Small angle X-ray scattering analyses was characterized with Xenocs SAXS equipment. The experiment was conducted in 1200s, under a power of 50 kV, 0.6 mA, using a PILATUS 100K detector and the wavelength was 0.15148. Positive ion MALDI (Matrix-Assisted Laser Desorption Ionization) TOF (Time of Flight) mass spectrometer measured on a Bruker Autoflex Speed MALDI TOF MS using dithranol as the matrix. Samples in water was combined with methanol containing dithranol molecules. FT-IR spectra were recorded at room temperature using a Thermo Nicolet Avatar 360 FTIR Spectrometer in the 400–4000 cm^{-1} range. Elemental analysis (EA) was performed using a European A3000 Elemental Analyzer. Thermogravimetric analysis (TGA) was performed using a TA Instruments Q50 TGA, with a Pt sample pan under 40 mL min^{-1} nitrogen purge. The sample was heated from room temperature to 800 °C at the rate of 20 °C/min. Differential scanning calorimetry (DSC) was performed using a TA Instruments Q1000@Mfg-dsc, with an Al hermetic sample pan under 40 mL min^{-1} nitrogen purge. The sample was heated from 40 °C to 600 °C at the rate of 10 °C/min. X-ray photoelectron spectroscopy (XPS) spectra were recorded using a Thermo Fisher Scientific Escalab 250. UV-visible (UV-Vis) spectra were measured using a Varian 50 BIO spectrophotometer. Crystals of **1** and **2** was suspended in 0.1 M aqueous acetate buffer at pH 6.07. The mixture was sonicated for 15 min at 45 °C to yield a yellow solution. The solution was filtered using a Whatman Puradisc 30 syringe filters (pore size 0.2 μm) and then subjected to UV-Vis analysis. Corresponding UV-Vis samples in acetate buffer (filtered

solution) were subjected to Dynamic light scattering (DLS) analysis with BECKMAN COULTER DelsaTM Nano C particle analyser. Scanning electron microscopy (SEM) images were obtained in field emission scanning electron microscope (FESEM; MERLIN Compact, Carl Zeiss) at an acceleration voltage of 200 kV. Corresponding UV-Vis and DLS samples in acetate buffer (filtered solution) were drop-casted on a silicon wafer following naturally drying and then washed with Milli-Q ultrapure water.

Single crystal X-ray diffraction data for **1** were collected on a Bruker Apex II diffractometer equipped with a CCD area detector using Mo-Kα radiation from a fine-focus sealed source with a focusing collimator (Bruker Nano). Data for **2** were collected on Bruker D8 Venture diffractometer with a Photon 100 CMOS area detector using Mo-Kα radiation (λ = 0.71073 Å) from an IμS microfocus source (Bruker Nano, Inc., Madison, WI, USA). Crystals were cooled to 100 K under a cold stream of N_2 gas using a Cryostream 700 cryostat for **1** (Oxford Cryosystems) and a Cryostream 800 cryostat (Oxford Cryosystems, Oxford, UK) for **2**. Hemispheres of unique data were collected using strategies of scans about the phi and omega axes. The Apex3 software suite was used for data collection, unit cell determination, data reduction, scaling, and absorption correction.[1]

Compound **1** was solved and refined using SHELXL-2017[2] and SHELXT[3] as the interface. The ordered portion of the structure was refined anisotropically. Some of the propanol chains were so strongly affected by disorder that no clear interpretation of the difference map was possible; however each PgC_3OH moiety has at least 1 fully ordered propanol chain which confirms the identity of the moiety. For the disordered chains, the closest reasonable difference map peaks were refined as propanol chains using distance and angle restraints. Atoms that gave clearly unrealistic geometries or displacement parameters were not given any riding hydrogen atoms. These atoms were left in the structure to help make the disordered solvent calculation more accurate and allow better visualization of the disordered regions. Compound **1** also showed difference map peaks inside the MONCs which closely resembled the expected geometry of a proline ligand, but attempts to refine this ligand failed to converge with a realistic geometry. Ultimately the entire proline moiety was modeled as a rigid group using coordinates from a published structure with a similar conformation[4] and using a single parameter to describe the atomic displacements for all ring carbon atoms. This refinement revealed that the proline ring was disordered over two conformations, both of which could be modeled with distance and angle restraints. The difference map also indicated the presence of a second unique proline molecule in the cavity, but not all atoms could be located. This molecule was ultimately excluded from the model and treated with

a solvent mask. *Olex2* v. 1.3.0 was used for model building and as an interface for SHELX.[5] PLATON SQUEEZE was used to implement solvent masks.[6] Literature coordinates were obtained from the Cambridge Crystallographic Data Center using the database searching software ConQuest V. 2.0.5.[7]

Compound **2** was solved by isomorphous replacement. The coordinates of the isomorphous Mg^{2+} analog[8] were used as an initial model with all Mg sites replaced with Mn. The structure was refined to convergence by full matrix least squares refinement against F^2 using SHELXL-2017.[2] The diffraction data for the crystal was essentially negligible beyond 1.1 angstroms (R_{int} > 50% for the 1.44-1.39 angstrom shell; average I/sigma at 1.10 is approximately 0.40). Due to the lower data-to-parameters ratio of the Mn^{2+} model caused by the weak diffraction, some disordered lattice solvent molecules from the Mg^{2+} model were removed using a solvent mask. The converged model (after solvent masking) has a GooF near 1 and a reasonably smooth residual difference map, both indicate the coordinates from the Mg^{2+}model agree well with the Mn^{2+} data. The presence of two lattice acetonitrile molecules from the Mg^{2+}model that refine well further supports that the packing in these two structures is almost identical. H atoms could not be located for O-H groups and were left out of the model but included in the formula. The identities of the axial ligands bound the Mn ions are uncertain from the X-ray diffraction data, so only the coordinating O atoms were included in the formula. The formula assumes that Mn^{2+} ions are charge balanced by deprotonated phenolic O-H groups.

2. Synthesis of *C*-propan-3-ol pyrogallol[4]arene (PgC_3OH).

C-propan-3-ol pyrogallol[4]arene **1** was prepared by a condensation reaction of pyrogallol and 2,3-Dihydrofuran catalyzed by concentrated hydrochloric acid.[9] 2,3-Dihydrofuran (6.05 mL, 0.08 mol), and pyrogallol (0.08 mmol, 10 g) were mixed in ethanol (40 mL) followed by the addition of 3.5 ml of concentrated HCl. Thereafter, the mixture was heated to reflux at 110 °C for 24 h. After cooling down, the precipitate was filtered, washed with cold ethanol and dried in vacuum. 5.4 g of white solid was collected as the final product. Yield is 34.8 %.

3. Investigations of reaction conditions of HSSs.

PgC_3OH (0.2 mmol), a source of Mn^{II} ions, $Mn(NO_3)_2$, $MnSO_4$ and $MnCl_2$ (0.8 mmol) and NaOMe (0.6 mmol) or triethylamine (112 µl, 0.8 mmol) were combined in DCM/MeOH (10 mL each). Upon slow evaporation of the mother liquor over six weeks, no MONCs-based crystals/precipitates were observed, but some dark insoluble MnO_2 was found to precipitate when utilizing $Mn(NO_3)_2$ as the source of Mn^{II}

ions. The formation of MnO_2 was confirmed by reaction with HCl which would lead to the formation of $MnCl_2$ crystals. This indicates that *in-situ* redox reactions may prevent the formation of HSSs, and that the formation of these highly intricate structures is unfavorable under ambient conditions, owing to their high structural strength. Efforts were then made to determine whether the formation of HSSs could be facilitated under solvothermal conditions. PgC_3OH (0.1 mmol, 78.4 mg) and manganese slats, including $Mn(NO_3)_2{\cdot}4H_2O$, $MnSO_4{\cdot}H_2O$ and $Mn(Cl)_2$ (0.4 mmol, 100.4 mg, 67.6 mg, 50.3 mg, respectively) were dissolved 1.5 mL of N,N-dimethylformamide (DMF), 1.5 mL of acetonitrile (CH_3CN) and 0.1 mL water, followed by the addition of 16 mg sodium methoxide (0.3 mmol). The mixture was sonicated for 30 min at 45 °C to yield a dark brown solution (final pH=4.47), and then heated at 80 °C for 12 hours. Dark insoluble MnO_2 precipitates and colorless block-like crystals of a well-known $Mn_3(HCOO)_6]^{\cdot}$ DMF metal-organic frameworks were obtained,[10] yield is 8 mg. The formation of either MnO_2 precipitation or a well-known $[Mn_3(HCOO)_6]$ metal-organic framework, implying that they compete with the selective assembly of Mn^{II}-seamed MONCs and HSSs.

4. Preparation and characterization of the HSSs crystals 1 and 2

Preparation of **1**.

PgC_3OH (0.1 mmol, 78.4 mg) and $Mn(NO_3)_2{\cdot}4H_2O$ (0.4 mmol, 100.4 mg) were dissolved 1.5 mL of N,N-dimethylformamide (DMF), 1.5 mL of acetonitrile (CH_3CN) and 0.1 mL water, followed by the addition of 36 mg L-proline (0.3 mmol). The mixture was sonicated for 30 min at 45 °C to yield a dark brown solution (final pH=4.13), and then heated at 80 °C for 12 hours. Large yellow block crystals were then formed and collected for single crystal X-ray analysis. Unit cells of several crystals (protected in oil) were checked in order to establish sample homogeneity. Yield: 68 mg=58% (with respect to PgC_3OH ligand). The crystals are sensitive to loss of solvent and exposure to air, and thus acquiring a suitable X-ray diffraction powder patterns were not successful. MALDI-TOF-MS: $[Mn_{24}(PgC_3OH)_6(H_2O)_{24}(Proline)_2]$, ideal $C_{250}H_{332}O_{140}N_2Mn_{24}$, m/z = 6945; found m/z = 6600-7500 Da. Elemental analysis (%): $[Mn_{24}(PgC_3OH)_6(H_2O)_{24}(Proline)_2]{\cdot}16(DMF){\cdot}8H_2O{\cdot}2CH_3CN$, ideal $C_{302}H_{446}O_{164}N_{20}Mn_{24}$: C, 43.45; H, 5.35; N, 3.36; Found: C, 43.27; H, 5.42; N, 3.45.

Crystallographic data for **1** (CCDC: 1981690): monoclinic, space group P21/n (No. 14), a = 22.3705 (17), b = 32.550 (2), c = 22.5838 (17) Å, β = 95.026 (2)°, V = 16381 (2) $Å^3$, Z = 2, Dc = 1.356 g cm^{-3}, F_{000} = 6824, Bruker APEX II area detector, MoKα radiation, λ = 0.71073 Å, T = 100.0 K, $2\theta_{max}$ = 46.8°, 223225 reflections collected, 23785 unique (R_{int} = 0.0810). Final GooF = 1.678, R1 = 0.1318, wR2 = 0.3823, R

indices based on 14496 reflections with I > 2σ (I) (refinement on F^2), 1581 parameters, 1534 restraints. Lp and absorption corrections applied, μ = 0.974 mm^{-1}.

Preparation of **2**.

PgC_3OH (0.1 mmol, 78.4 mg) and $Mn(NO_3)_2{\cdot}4H_2O$ (0.4 mmol, 100.4 mg) were dissolved 1 mL of N,N-dimethylformamide (DMF) and 2 mL of acetonitrile (CH_3CN) with the addition of 0.5 ml of water and 36 mg L-proline (0.3 mmol) in a 4 ml glass vial (final pH=4.2). The mixture was sonicated for 30 min at 45 °C to yield a dark brown solution, and then heated at 130 °C for 12 hours. Large orange block crystals were then formed and collected for single crystal X-ray analysis. Unit cells of several crystals were checked in order to establish sample homogeneity. Yield: 70 mg=61% (with respect to PgC_3OH ligand). MALDI-TOF-MS: $[Mn_{24}(PgC_3OH)_6(H_2O)_{44}]$, ideal $C_{240}H_{324}O_{140}Mn_{24}$, m/z = 6765; found m/z = 6500-7700 Da. Elemental analysis (%): $[Mn_{24}(PgC_3OH)_6(H_2O)_{44}]{\cdot}14(DMF){\cdot}10H_2O{\cdot}2CH_3CN$, ideal $C_{290}H_{454}O_{164}N_{18}Mn_{24}$: C, 42.83; H, 5.58; N, 3.11. Found: C, 42.67; H, 5.27; N, 3.16.

Crystallographic data for **2** (CCDC: 1981691): orthorhombic, space group Pccn (No. 56), a = 37.471 (5), b = 39.182 (5), c = 25.613 (4) Å, V = 37604 (9) $Å^3$, Z = 4, Dc = 1.209 g cm^{-3}, F_{000} = 13952, Bruker VENTURE CMOS area detector, MoKα radiation, λ = 0.71073 Å, T = 100.0 K, $2\theta_{max}$ = 37.8°, 164260 reflections collected, 14844 unique (R_{int} = 0.2472). Final GooF = 1.013, R1 = 0.0858, wR2 = 0.2134, R indices based on 7398 reflections with I > 2σ (I) (refinement on F^2), 1843 parameters, 1961 restraints. Lp and absorption corrections applied, μ = 0.852 mm^{-1}.

Manganese Bond-Valence Sum (BVS) Analysis

Table S1. Bond-valence sum analysis for Mn1-Mn12 in **1** and their corresponding oxidation state assignments.[11]

Identity	Calculated Value	Assignment
Mn1	2.179	+2
Mn2	2.147	+2
Mn3	2.159	+2
Mn4	2.076	+2
Mn5	1.832	+2
Mn6	2.118	+2
Mn7	2.048	+2
Mn8	1.824	+2
Mn9	2.171	+2
Mn10	2.222	+2

Mn11	2.046	+2
Mn12	2.384	+2

Table S2. Bond-valence sum analysis for Mn1-Mn12 in **2** and their corresponding oxidation state assignments.

Identity	Calculated Value	Assignment
Mn1	2.167	+2
Mn2	2.199	+2
Mn3	2.066	+2
Mn4	2.404	+2
Mn5	2.320	+2
Mn6	2.251	+2
Mn7	2.207	+2
Mn8	2.331	+2
Mn9	2.265	+2
Mn10	2.192	+2
Mn11	2.234	+2
Mn12	2.352	+2

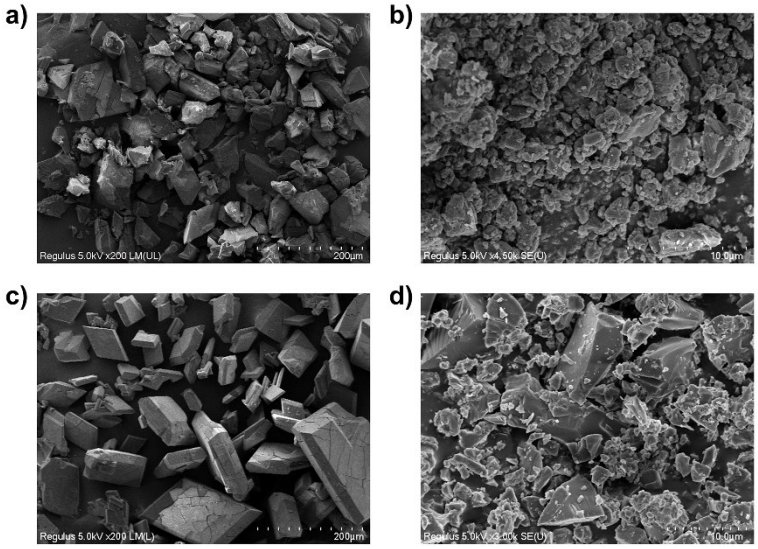

Figure S1. SEM images of **1** (a), (b) and **2** (c), (b).

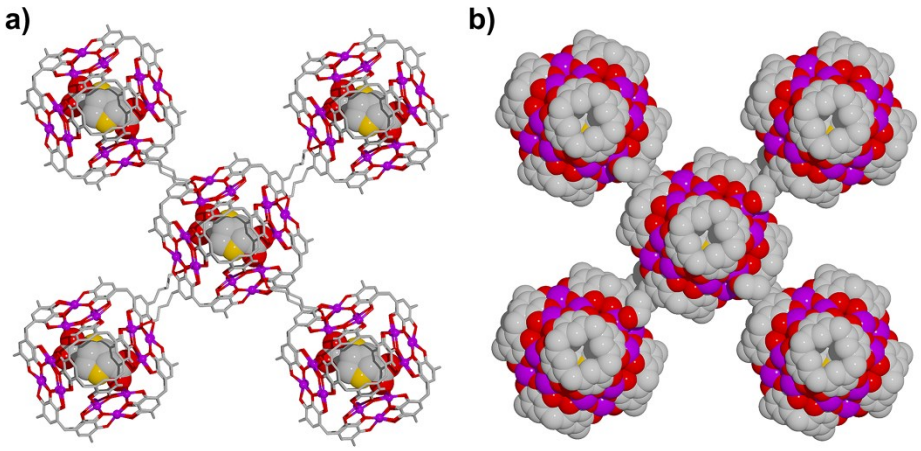

Figure S2. Side views of a) stick and b) space-filling model and of **1.** Color codes: manganese atoms are green; carbon atoms are yellow; oxygen atoms are red; nitrogen atoms are orange. Hydrogen atoms, axial water ligands, and hydroxyl alkyl chains of PgC_3OH were removed for clarity. The proline molecule itself can form stable metal complexes with Mn^{II}, this may be attributed to it contains both carboxyl groups and N-heterocycle substituents belonging to amino acid residues of manganese proteins, which have been shown high affinity for coordinating and stabilizing Mn^{II} ions.[12]

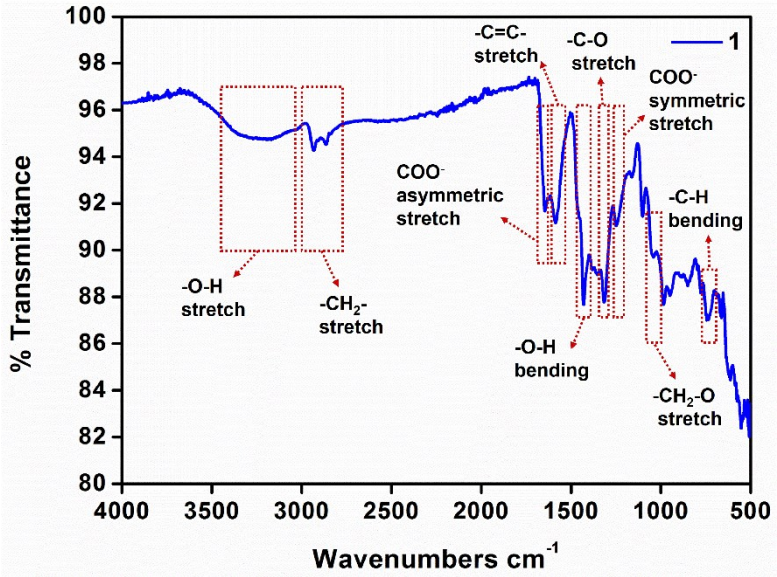

Figure S3. FTIR spectra of **1**. The absorption peaks of the stretching vibration bands derived from -CH2-, -COO-, -C-O, -OH and benzene ring on proline and PgC_3OH were observed in FTIR spectra.

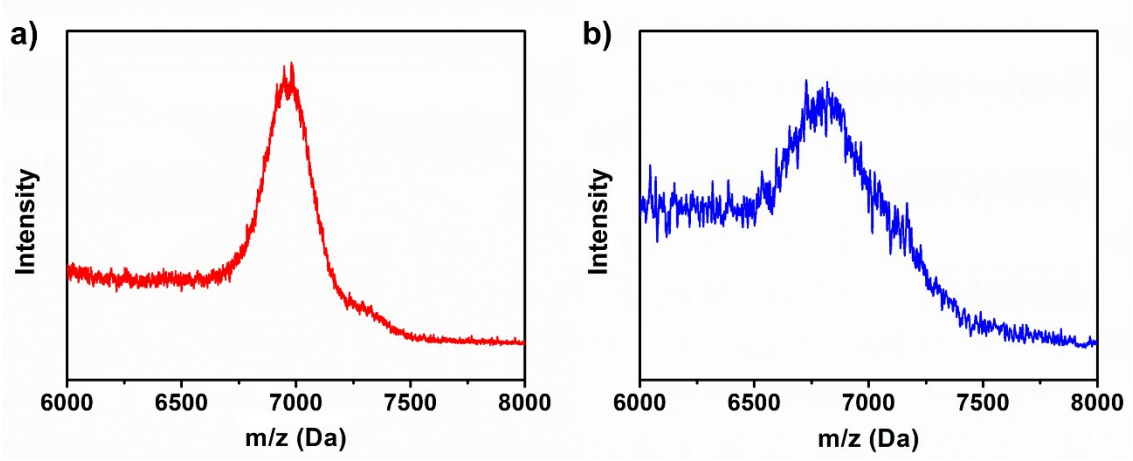

Figure S4. MALDI-TOF spectrum for **1** (a) and **2** (b) in methanol/water (1:1). The spectrum was obtained by using dithranol as the matrix.

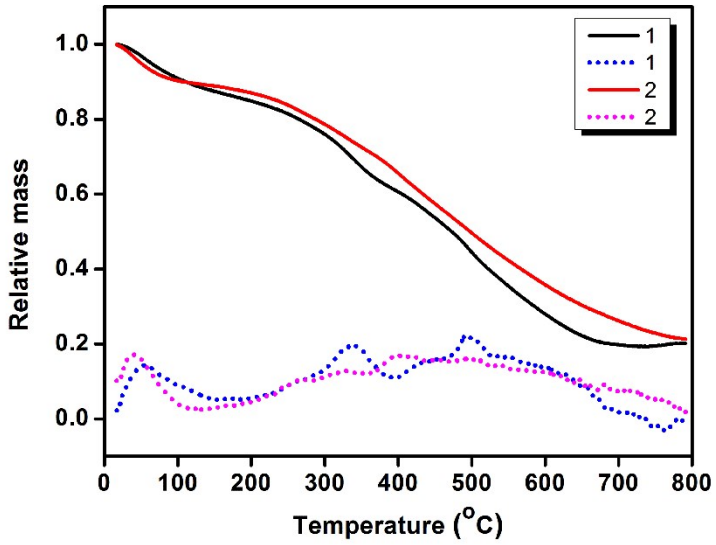

Figure S5. Thermogravimetric Analysis (TGA) Graphs (solid lines) and its first derivative value (dash lines) of **1** and **2**, showing three major distinct stages during gradual heating of a dried sample. 1) loss of trapped solvent molecules at around 100 °C; 2) breaking of crystal lattice, release of axial ligands and encapsulated solvent molecules within MONC subunits at around 320 °C; and 3) decomposition of the MONC subunits at around 500 °C.

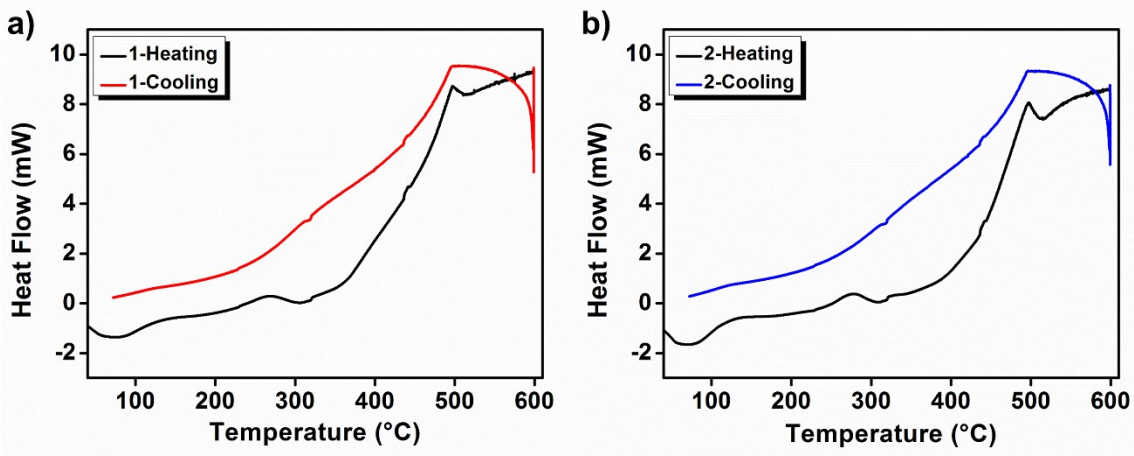

Figure S6. Differential scanning calorimetry (DSC) Graphs of (a) **1** and (b) **2**, indicating that solvent loss begins at around 40 °C (negative slope at the very beginning indicates an endothermic process). This continues until about 320 °C when the heat flow goes from negative (endothermic) to positive (exothermic), which suggests that at this point the crystal is reacting chemically. By 500 °C the reaction is complete.

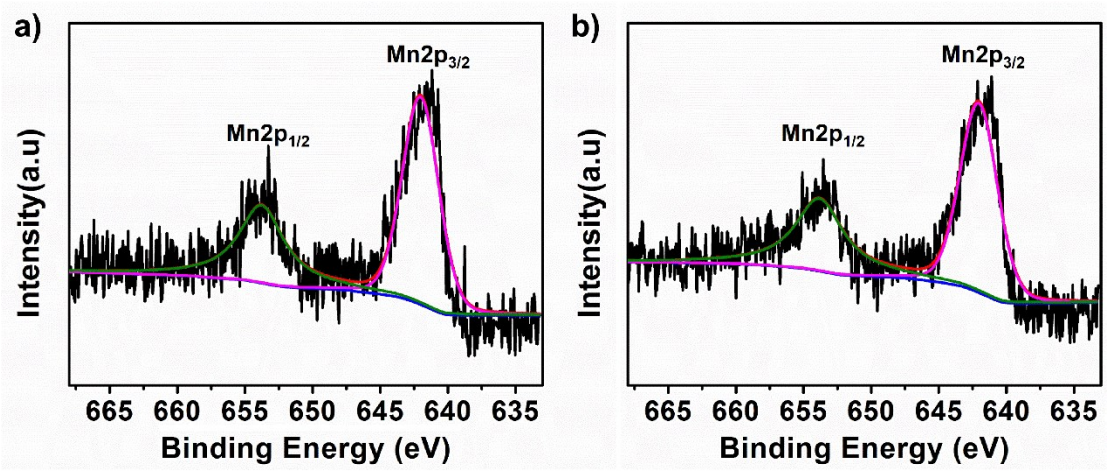

Figure S7. Mn2p XPS spectrum of **1** (a) and **2** (b). The XPS spectrum of **1** and **2** only illustrated the presence of Mn^{II} ions with two sharp Mn $2p_{3/2}$ and Mn $2p_{1/2}$ signals at 642.0 eV and 653.8 eV for **1**, 642.1 eV and 653.9 eV for **2**, respectively.[13]

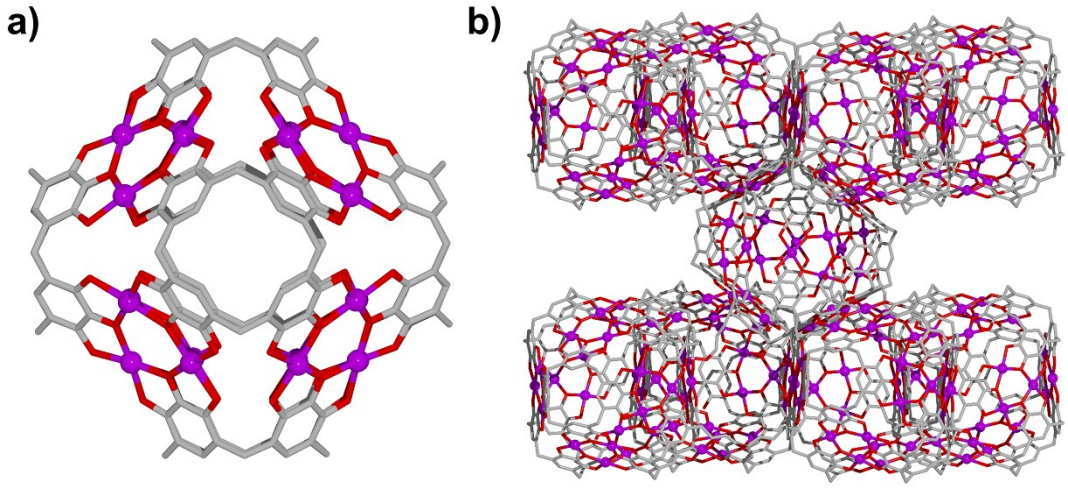

Figure S8. Crystal structure of a) MONC subunits (secondary structure) and b) supramolecular nanocubes (tertiary structure) within **2**. Color codes: manganese (purple), carbon (grey), oxygen (red). Hydrogen atoms, axial ligands and hydroxyl tail alkyl chains not involved in metal–ligand coordination to adjacent MONC subunits were removed for clarity. Proline molecules could not be explicitly modeled in the crystal structure, but they are essential for the synthesis.

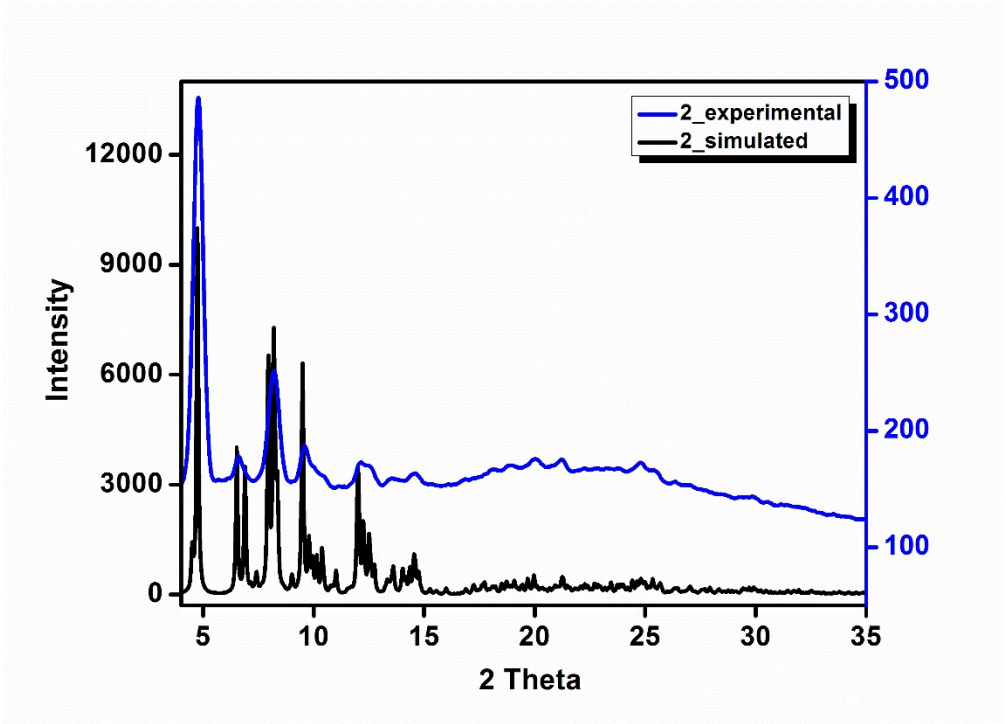

Figure S9. Simulated and experimental powder X-ray Diffraction patterns of **2**, showing high crystal stability, which the PXRD pattern of **2** matches well with the simulated pattern. This observation suggests that, construction of 3D frameworks using these MONCs as subunits may be an alternative way to characterize and study their structures.

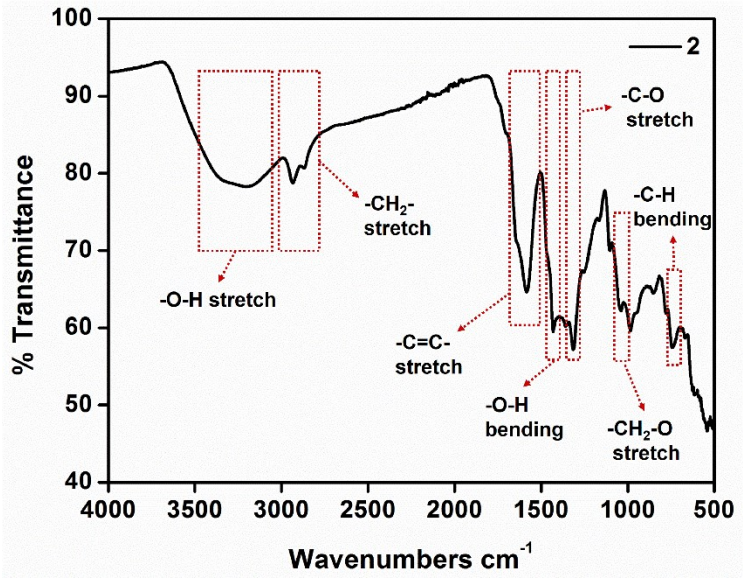

Figure S10. FTIR spectra of solid **2**. The absorption peaks of the stretching vibration bands derived from -CH2-, -CO, -OH and benzene ring on PgC_3OH were observed in FTIR spectra.

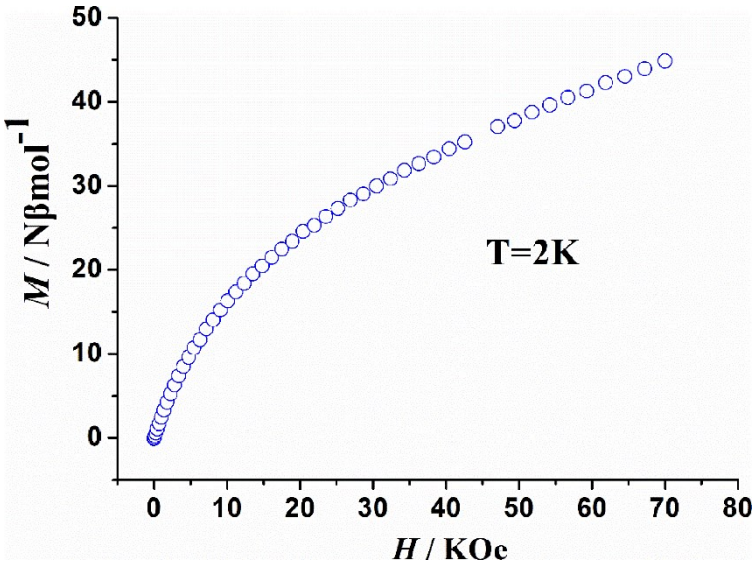

Figure S11. Magnetization analysis for compound **1**. Magnetization (*M*) vs. field (*H*) for **1** in the indicated field.

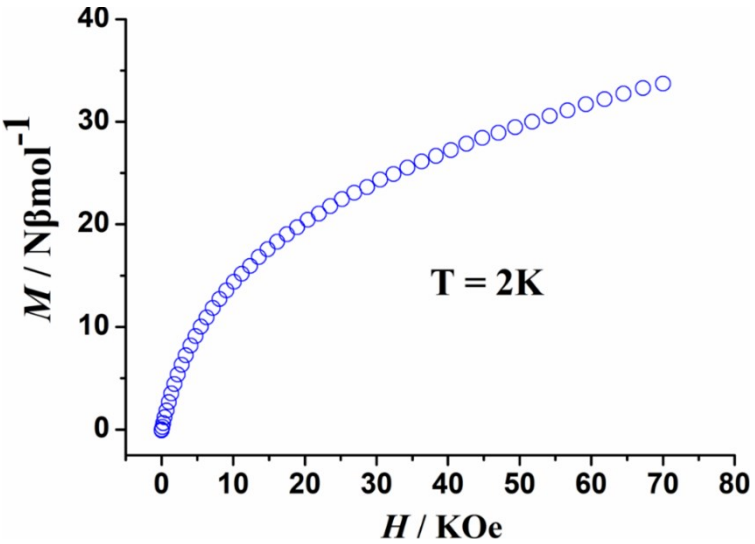

Figure S12. Magnetization analysis for compound **2**. Magnetization (*M*) vs. field (*H*) for **2** in the indicated field.

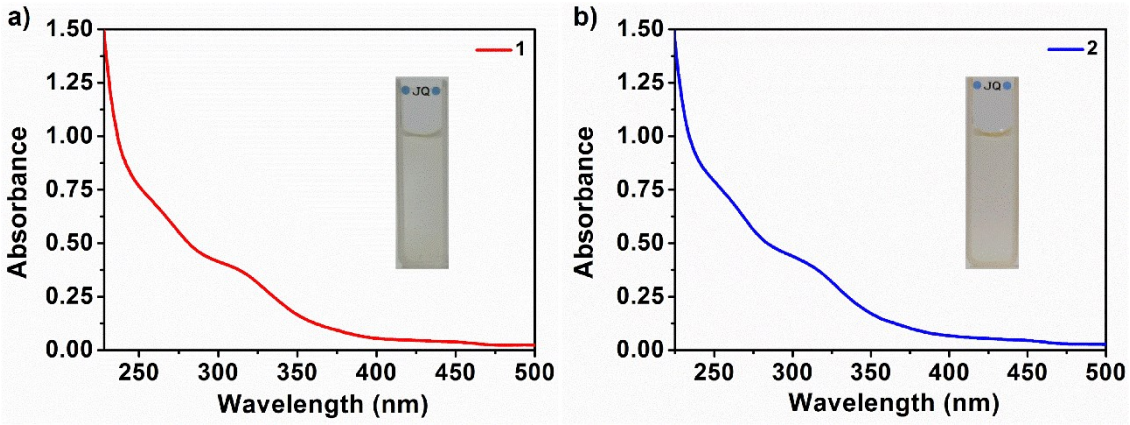

Figure S13. UV-vis spectra and photograph of **1** (a) and **2** (b) in 0.1 M acetate buffer at pH 6.07.

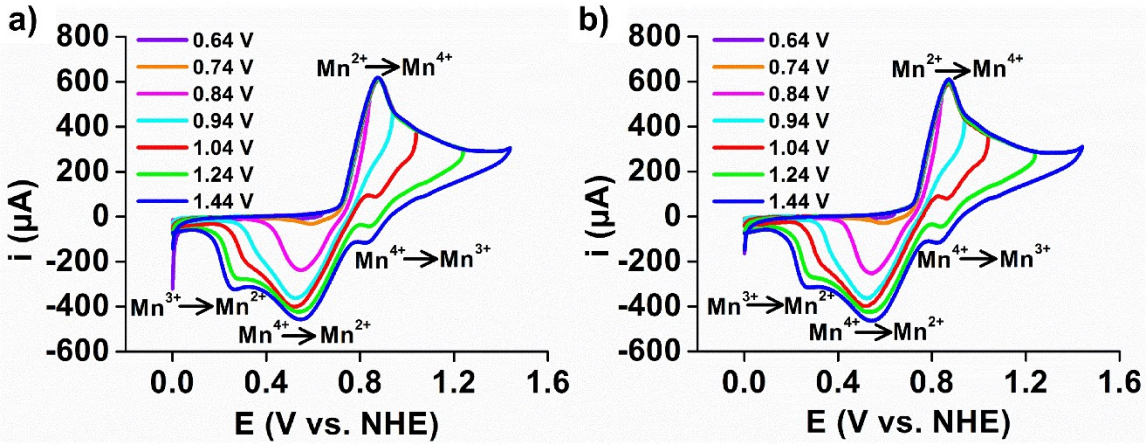

Figure S14. CV scans of **1** (a) and **2** (b) (0.5 mM, 50 mV s^{-1} scan rate) in 0.1 M acetate buffer at pH 6.07 taken at different potential ranges.

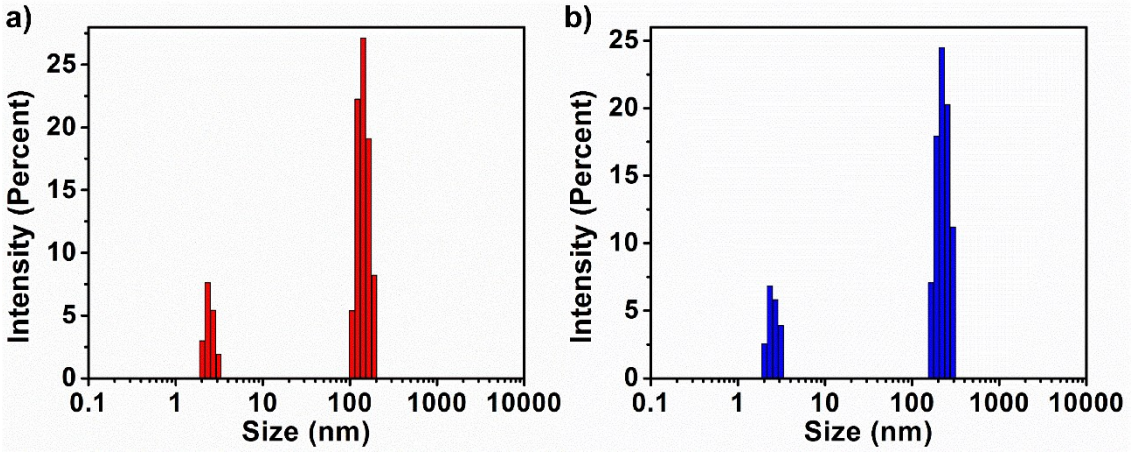

Figure S15. DLS measurements for **1** (a) and **2** (b) 0.1 M acetate buffer at pH 6.07 (0.5 mM). The DLS analysis of **1** and **2** indicated the existence of individual MONCs (molecular hydrodynamic diameter: 2-3 nm). This observation suggests that, in aqueous acetate buffer, the HSSs converted into discrete MONCs and these MONCs tend to exist as large aggregates.

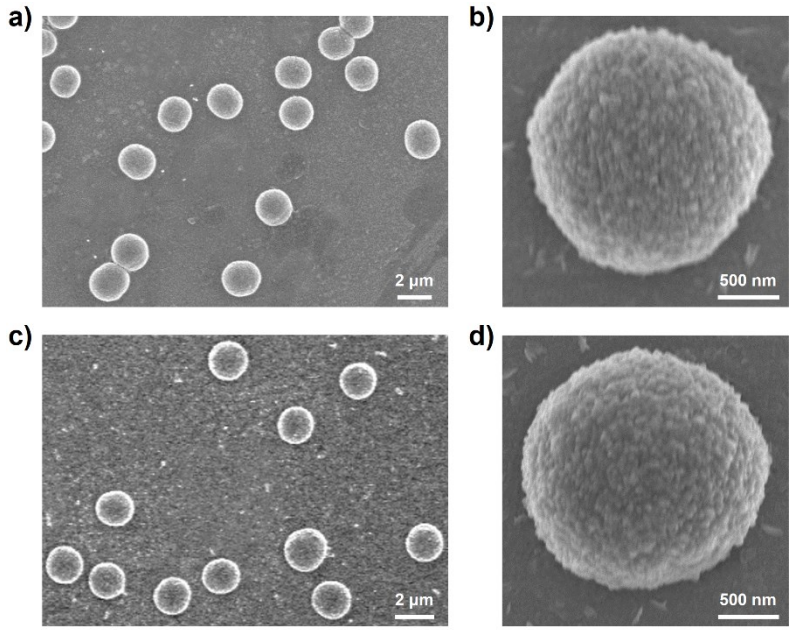

Figure S16. SEM images of micron spheres of 1 (a, b) and 2 (c, d) in 0.1 M acetate buffer at pH 6.07 (0.5 mM).

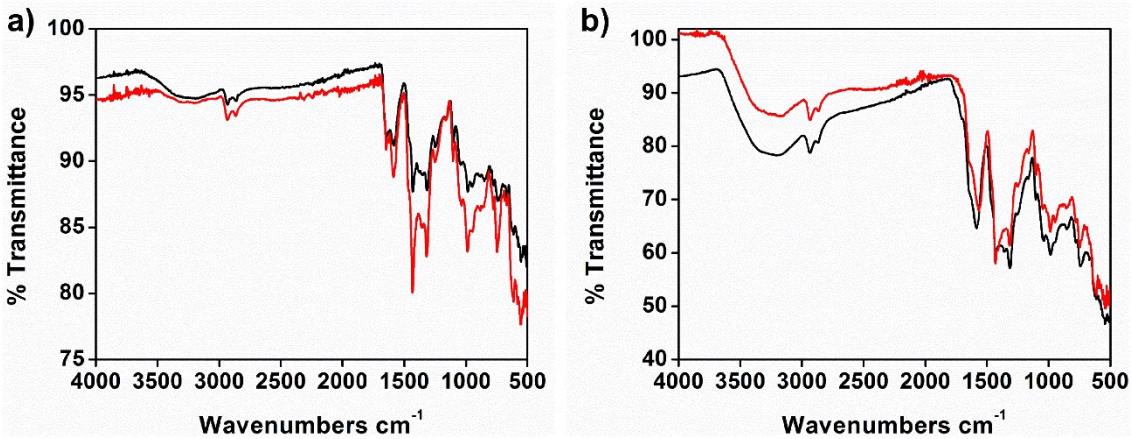

Figure S17. FT-IR spectra of **1** (a) and **2** (b) before (black lines) and after (red lines) dissolved in 0.1 M acetate buffer at pH 6.07 for two weeks (0.5 mM). These results indicate the existence of individual MONCs.

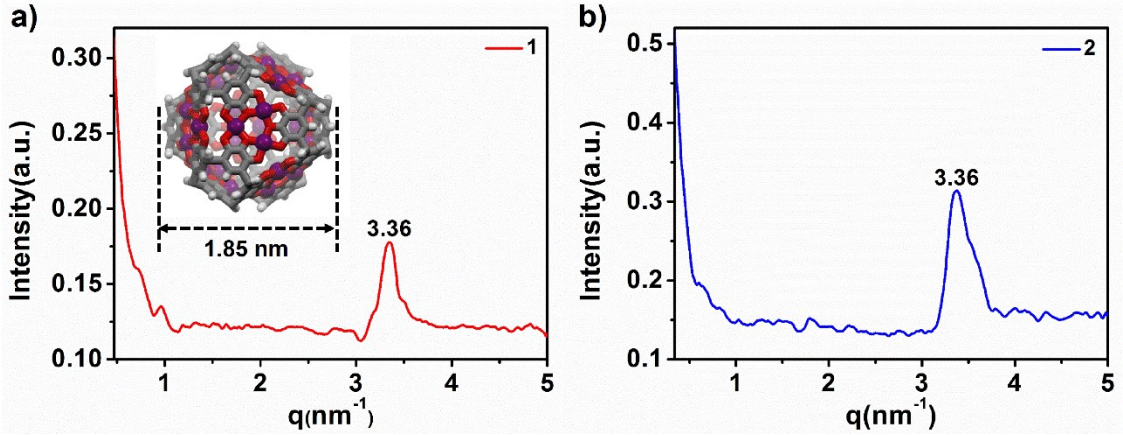

Figure S18. Small-Angle X-ray Scattering (SAXS) analysis of **1** (a) and **2** (b) after dissolved in 0.1 M acetate buffer at pH 6.07 for two weeks (0.5 mM). The broad peaks at scattering vector q =3.36 nm^{-1}, correspond to the spherical nanostructure with a diameter of 1.87 nm, which were assigned to the size of individual MONCs.[15]

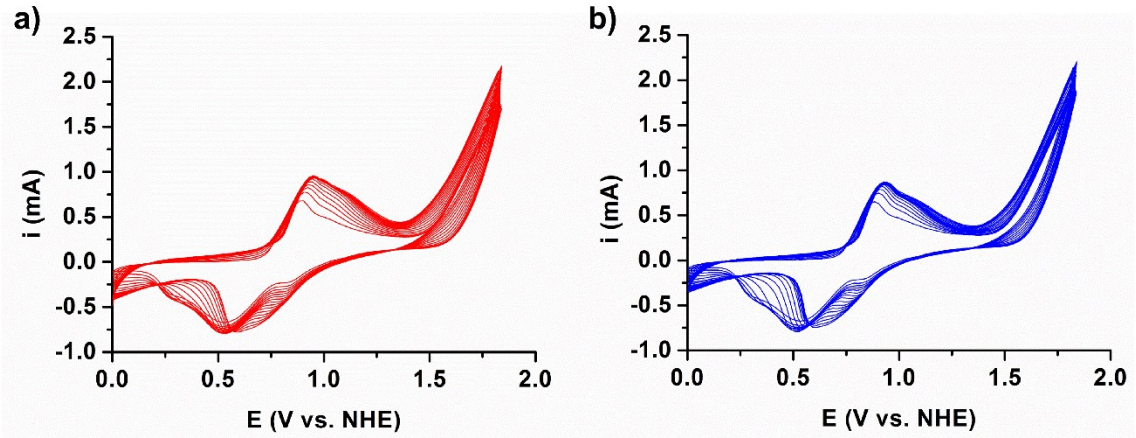

Figure S19. Continuous 30 CVs of **1** (a) and **2** (b) (0.5 mM, 50 mV s^{-1} scan rate) in 0.1 M acetate buffer at pH 6.07 using FTO as the working electrode. The catalytic current does not increase over successive cyclic voltammetric (CV) scans. A crossover profile with a re-reduction wave in the reverse CV scan was not observed. These observations suggest that MONC subunit is a homogeneous catalyst for water oxidation.[14]

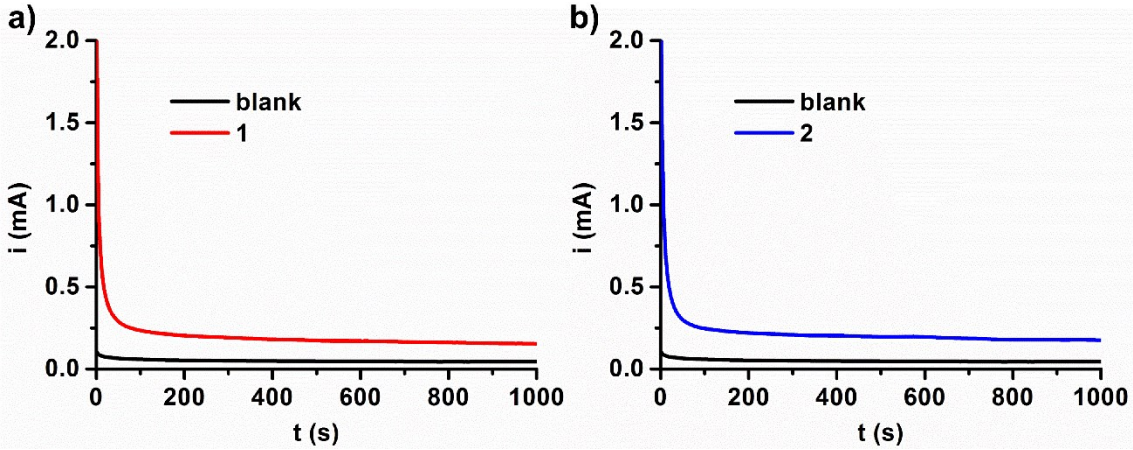

Figure S20. Bulk electrolysis at 1.79 V vs. NHE of 1 mM **1** (a) and **2** (b) in 0.1 M acetate buffer at pH 6.07 using FTO as the working electrode. For comparison, bulk electrolysis of the blank buffer is also performed. The catalytic current does not increase, as would be expected for a heterogeneous catalytic system.

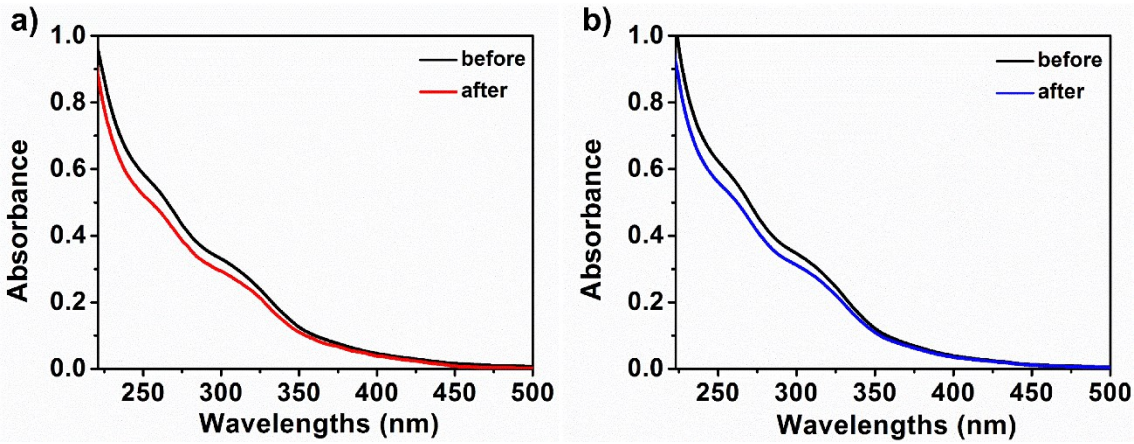

Figure S21. UV-vis spectra of **1** (a) and **2** (b) in 0.1 M acetate buffer at pH 6.07 after electrolysis. No new bands are observed, suggesting that the formation of new species is unlikely.

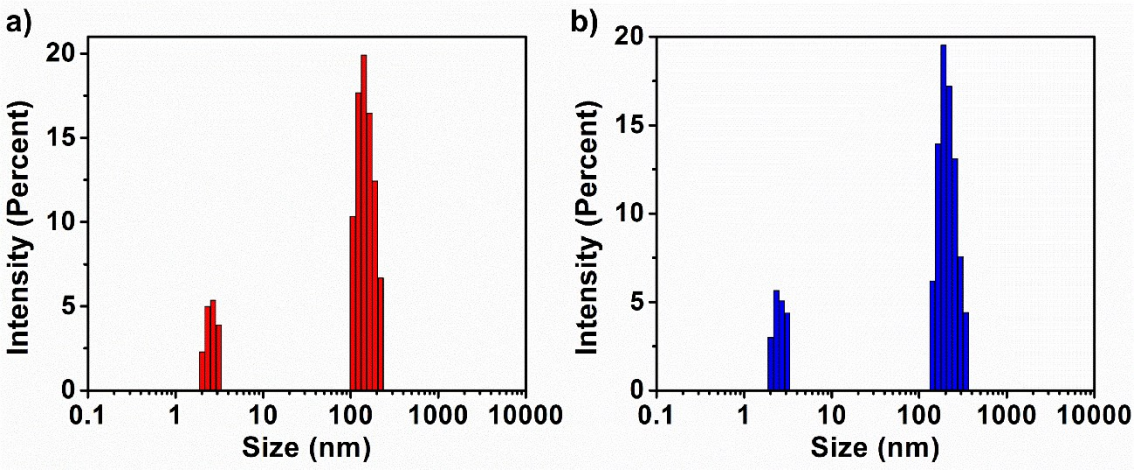

Figure S22. DLS measurements for **1** (a) and **2** (b) in 0.1 M acetate buffer at pH 6.07 after electrolysis.

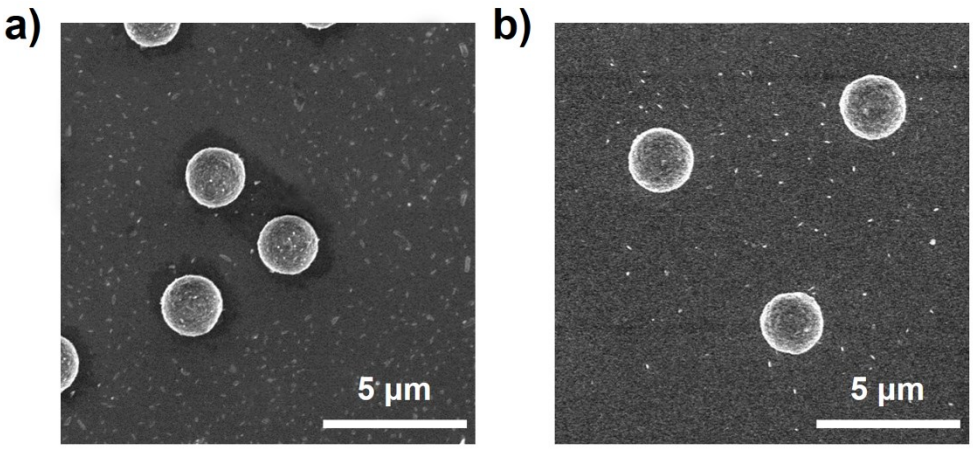

Figure S23. SEM images of **1** (a) and **2** (b) in 0.1 M acetate buffer at pH 6.07 after electrolysis.

References

[1] Apex3, AXScale, and SAINT, version 2017.3-0, Bruker AXS, Inc., Madison, WI, 2017.

[2] G. M. Sheldrick, *Acta Cryst. Sect. C: Struct. Chem.*, 2015, **71**, 3-8.

[3] G. M. Sheldrick, *Acta Cryst. Sect. A. Found. Adv.*, 2015, **71**, 3-8.

[4] N. Tumanova, N. Tumanov, F. Fischer, F. Morelle, V. Ban, K. Robeyns, Y. Filinchuk, J. Wouters, F. Emmerling and T. Leyssens, *CrystEngComm*, 2018, **20**, 7308-7321.

[5] O. V. Dolomanov, L. J. Bourhis, R. J. Gildea, J. A. K. Howard and H. Puschmann, *J. Appl. Cryst.*, 2009, **42**, 339-341.

[6] A. L. Spek, *Acta Cryst. Sect. C. Struct. Chem.*, 2015, **71**, 9-18.

[7] C. Zhang, F. Wang, R. S. Patil, C. L. Barnes, T. Li and J. L. Atwood, *Chem. Eur. J.*, 2018, **24**, 14335-14340.

[8] I. J. Bruno, J. C. Cole, P. R. Edgingtion, M. Kessler, C. F. Macrae, P. McCabe, J. Pearson and R. Taylor, *Acta Cryst. Sect. B. Struct. Sci.*, 2002, **58**, 389-397.

[9] B. C. Gibb, R. G. Chapman and J. C. Sherman, J. Org. Chem. 1996, **61,** 1505-1509.

[10] K. H. Li, D. H. Olson, J. Y. Lee, W. H. Bi, K. Wu, T. Yuen, Q. Xu and J. Li, *Adv. Funct. Mater.*, 2008, **18**, 2205.

[11] a) I. Brown and D. Altermatt, *Acta Cryst. B*, 1985, **41**, 244-247; b) V. Sidey, *Acta Cryst. B*, 2014, **70**, 608-611.

[12] a) B. Weeraswami, P. Bhushanavathi, U. Viplavaprasad and G. N Rao, *Chem. Spec. Bioavailab*., 2013, **25**, 1-5; b) D. Lu, M. E. Wörmann, X. Zhang, O. Schneewind, A. Gründling and P. S. Freemont, *Proc. Natl. Acad. Sci. U.S.A.*, 2009, **106**, 1584-1589.

[13] D. Bansal, A. Mondal, N. Lakshminarasimhan and R. Gupta, *Dalton Trans.*, 2019, **48**, 7918-7927.

[14] J. Li, A. Jiao, S. Chen, Z. Wu, E. Xu and Z. Jin, *J. Mol. Struct.*, 2018, **1165**, 391-100.

[15] a) L. Zhu, J. Du, S. Zuo and Z. Chen, *Inorg. Chem.*, 2016, **55**, 7135−7140; b) J. Du, Z. Chen, S. Ye, B. J. Wiley and T. J. Meyer, *Angew. Chem. Int. Ed*., 2015, **54**, 2073-2078.